ROYAL SOCIETY OPEN SCIENCE

royalsocietypublishing.org/journal/rsos

Research

Cite this article: Stepinski TF, Nowosad J. 2023 The kinetic Ising model encapsulates essential dynamics of land pattern change. *R. Soc. Open Sci.* **10**: 231005.
https://doi.org/10.1098/rsos.231005

Received: 18 July 2023
Accepted: 2 October 2023

Subject Category:
Ecology, conservation and global change biology

Subject Areas:
ecology/environmental science/statistical physics

Keywords:
kinetic Ising model, land change, pattern evolution, Monte Carlo simulations

Author for correspondence:
Tomasz F. Stepinski
e-mail: stepintz@uc.edu

The kinetic Ising model encapsulates essential dynamics of land pattern change

Tomasz F. Stepinski[1] and Jakub Nowosad[2]

[1]Space Informatics Lab, Department of Geography and GIS, University of Cincinnati, Cincinnati, OH 45221-0131, USA
[2]Institute of Geoecology and Geoinformation, Adam Mickiewicz University, Poznan, Poland

TFS, 0000-0001-6818-203X

A land pattern change represents a globally significant trend with implications for the environment, climate and societal well-being. While various methods have been developed to predict land change, our understanding of the underlying change processes remains inadequate. To address this issue, we investigate the suitability of the two-dimensional kinetic Ising model (IM), an idealized model from statistical mechanics, for simulating land change dynamics. We test the IM on a variety of patterns, each with different focus land type. Specifically, we investigate four sites characterized by distinct patterns, presumably driven by different physical processes. Each site is observed on eight occasions between 2001 and 2019. Given the observed pattern at the time t_i we find two parameters of the IM such that the model-evolved land pattern at t_{i+1} resembles the observed land pattern at that time. The data support simulating seven such transitions per site. Our findings indicate that the IM produces approximate matches to the observed patterns in terms of layout, composition, texture and patch size distributions. Notably, the IM simulations even achieve a high degree of cell-scale pattern accuracy in two of the sites. Nevertheless, the IM has certain limitations, including its inability to model linear features, account for the formation of new large patches and handle pattern shifts.

1. Introduction

Land change studies have gained significant attention due to the accelerated transformation of Earth's land compared to previous years [1]. Over the past few decades, remote sensing of the land surface from space has provided insights into this global environmental trend [2], which affects a vast majority of landmasses and various land themes. Among these themes, tropical forest

THE ROYAL SOCIETY PUBLISHING

deforestation stands out as the most profoundly impacted [3]. The term 'land theme' means a specific land cover type whose change is investigated.

The acceleration of land change can be attributed, directly or indirectly, to anthropogenic impacts [4]. Consequently, global society holds the potential to intervene and mitigate, or even reverse, this trend. However, effective action requires accurate assessments of observed changes and reliable predictions of future changes. To address these requirements, a multitude of methods have been developed to assess the magnitude of past land change [5,6] and predict future changes [7,8]. The majority of these prediction methods adopt an empirical approach, extrapolating change patterns observed in the past while assuming constraints on future rates of change [9]. However, this research approach does not establish a causal link between the driving factors (causes) and the resulting patterns of land change (effects).

Causality is of interest in the field of landscape ecology, where the cause and effect are often referred to as the process (the forces acting on the land) and the pattern (the resulting landscape mosaic influenced by these forces) [10]. This necessitates the use of deterministic or agent-based modelling approaches. Deterministic models [11–13] simulate the impacts of environmental and anthropogenic processes on land patterns through mathematical descriptions of actual processes. On the other hand, agent-based models [14] simulate the behaviour of individual agents (e.g. farmers, developers or land managers) who interact with each other and their environment, resulting in changes to land patterns. However, a challenge associated with both deterministic and agent-based models lies in accounting for the multitude of potential forces and their interactions. Consequently, constructing and testing such models becomes a complex task due to the large number of free parameters involved.

To facilitate progress, a causal model can be substituted with an idealized model that retains simplicity for analysis or simulation purposes while capturing the fundamental aspects of the observed phenomenon. Within the realm of ecology, these models are known as neutral models of land change [15–17]. Neutral models are typically stochastic in nature, where the resulting land pattern emerges from the collective influence of random processes acting on small length scale.

This paper aims to assess the applicability of the Ising model (IM) [18–21], a neutral model, as a tool for simulating land change. In this context, the term 'land' refers to a pattern of land cover types assigned to cells, which are the smallest square-shaped plots of land arranged in a two-dimensional grid. A 'site' represents a specific tract of land corresponding to the entire grid. 'Land change' specifically denotes alterations in the pattern of a site over time. It is important to note that our concept of land change aligns with the remote sensing notion of land use/land cover (LULC) change [22].

The IM, initially introduced as a model for magnetic substances, has found applications beyond physics, extending into disciplines such as social science [23,24], psychology [25,26], genetics [27], environment [28], and, notably for this paper, ecology. In the field of ecology, the IM has been employed to investigate various phenomena, including the study of forest canopy-gap structure [29–31], modelling vegetation patterns along a regional rainfall gradient in southern Africa [32], analysing population dynamics [33] and elucidating emergent behaviours like masting [34].

In a recent study by Stepinski [35], the IM was examined as a model for the transition from completely forested to fully agricultural land. However, it is important to note that this model was not explicitly kinetic, focused solely on one thematic context, and assessed the model's time series using reconstructed patterns from multiple sites rather than using a time series of landscapes from a single site.

Our objective is to explore the suitability of the IM as a simplified representation of various real-life processes responsible for binary land change. Although focusing on binary patterns may appear restrictive, this choice is driven by the capabilities of the IM and the specific interests within the field. Many studies in LULC change analysis involve examining the changes within a particular LULC category, such as deforestation [36], urbanization [37], desertification [38] or wetland loss [39]. In such applications, the focus is typically on two categories: the foreground, representing the category under investigation for its pattern change, and the background.

It is essential to note that our investigation does not aim to utilize the IM as a tool for predicting future patterns with high cell-level accuracy, nor do we consider it a competitor to empirical predictors. Instead, our focus is on evaluating the feasibility of the IM as a basic dynamic process for simulating land change. While the simulated patterns need to match observations, this matching does not necessarily require high cell-level accuracy.

The IM itself does not inherently possess any predefined dynamics. Therefore, most previous applications of the IM in ecology have mainly focused on using the IM to simulate equilibrium (steady-state) land patterns and comparing them with observations obtained at a single point in time. The exception to this trend is the study by Nareddy *et al.* [33], who used a kinetic IM (they referred to

it as a dynamical IM) to simulate metapopulation dynamics. In our context, real land patterns do not exist in a steady state. Multiple observations over time demonstrate that land patterns undergo changes on various time scales, influenced by spatial scale and thematic content [6]. Thus, we use a kinetic IM, which enables the simulation of a time-dependent evolution of land patterns. The kinetic IM refers to the IM with a simply defined temporal evolution rule incorporated.

In order to evaluate the effectiveness of the IM in simulating the evolution of binary land patterns, we selected four specific sites that have undergone land cover changes associated with the loss or gain of distinct LULC categories. These categories include forest (reforestation), crops (expansion of croplands), wetlands (loss of wetland) and barren land (expansion of open-pit mining). The data for these sites were obtained from the National Land Cover Dataset 2019 (NLCD2019) [40]. The NLCD2019 provides maps of 16 land cover categories for the conterminous USA at a 30-m resolution for the years 2001, 2004, 2006, 2008, 2011, 2013, 2016 and 2019. By using our IM-based simulator, we were able to identify the best-fit time series of simulated patterns for these selected sites and subsequently compared them to the corresponding observed patterns.

2. Model description

The IM is grounded in the principles of statistical mechanics and energy minimization. In the IM, a site is represented by a rectangular array of cells with dimensions $d_1 \times d_2$. For the sake of simplicity, we assume square sites in this paper, hence $d_1 = d_2 = d$ and the total number of cells is denoted as $n = d^2$. Each cell in the IM is assigned to one of two categories: cells corresponding to the focus category of LULC are assigned a value of 1, while cells representing the background category are assigned a value of −1. In our figures, we consistently depict focus cells as green and background cells as yellow.

The IM assumes that a cell interacts solely with its four nearest neighbours (up, right, down and left from the focus cell). Additionally, the cell is influenced by an external force. The specific configuration of the array, denoted as ω_s, represents the land's pattern. Each specific pattern is associated with an energy value, denoted as $E(\omega_s)$:

$$E(\omega_s) = -\sum_{k\sim\ell}^{n} J\, x_{s,k}\, x_{s,\ell} - \sum_{k=1}^{n} B\, x_{s,k}. \tag{2.1}$$

In equation (2.1), $x_{s,k}$ represents the category of the kth cell in pattern ω_s. The first term on the right-hand side of equation (2.1) corresponds to an interaction term, with the symbol $k \sim \ell$ indicating summation over all neighbours in the array. This term captures the propensity for neighbouring cells to belong to the same category. The dimensionless parameter J denotes the strength of this propensity. In the context of land science, the first term accounts for a degree of the spatial autocorrelation of the landscape.

The second term on the right-hand side of equation (2.1) represents the response of a cell to an externally imposed force, favouring either the focus category (with a positive value of B) or the background category (with a negative value of B). The dimensionless parameter B quantifies the strength of this external force. It is important to note that x, J and B are all dimensionless. Consequently, $E(\omega_s)$ is a dimensionless fitness function, referred to as 'energy' for historical reasons. The parameters B and J are assumed to have uniform values across the entire array.

The original IM includes a third parameter known as temperature, denoted as T. However, in numerous non-physics applications of the IM, specifying an equivalent temperature parameter is often challenging. In these cases, the temperature can be understood as representing the willingness or ability of the pattern to deviate from its lowest energy state, potentially accounting for environmental noise [41]. In our study, we assume the temperature to be an unspecified constant that is incorporated into the definitions of J, B and $E(\omega_s)$.

Spatial autocorrelation-causing forces and external force are generic concepts that can be interpreted differently depending on the thematic context. The spatial autocorrelation process can manifest in various ways [42]. For instance, (a) land-use decisions, such as converting natural vegetation to croplands or urban areas, often lead to autocorrelation due to logistical considerations. (b) Spatial diffusion, such as the spread of invasive species or diseases from one area to another, can also contribute to autocorrelation. (c) Spatial feedback mechanisms, such as the interaction between neighbouring ecosystems, can further influence autocorrelation patterns [43]. Similarly, a category-favouring force can arise through different mechanisms. Examples include (a) the influence of physical and environmental factors on land cover, (b) the impact of business or political decisions on land-use patterns and (c) land

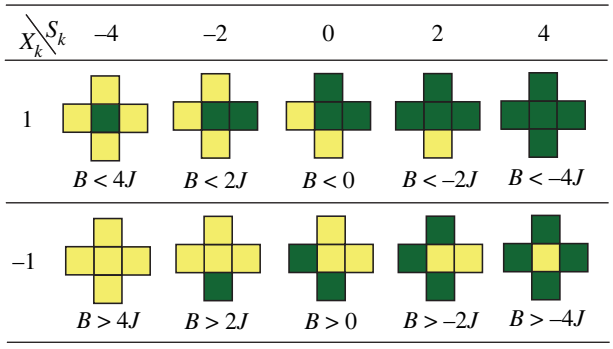

Figure 1. Ten possible types of neighbourhoods in the IM. If a condition below a neighbourhood is met, the central cell has a high probability of flipping.

conservation or restoration policies shaping the distribution of land cover categories. The specific nature of the force depends on the context and underlying factors driving land change.

For a given set of values for J and B, the initial pattern undergoes evolution towards the land pattern that minimizes $E(\omega_s)$. This is because the minimization of free energy is the fundamental principle driving the behaviour of physical systems [44,45], and because, in the case of the IM, $E(\omega_s)$ is a key component of the free energy. However, as mentioned in the Introduction, the IM itself does not provide a description of how this evolution occurs, necessitating the inclusion of a temporal evolution rule. In the literature, three different temporal evolution rules have been proposed for the IM: the Metropolis dynamics [46], the Glauber dynamics [47] and probabilistic cellular automata dynamics [48,49]. In this study, we employ the single-flip Glauber dynamics with periodic boundary conditions (which makes the grid topologically equivalent to a torus) to simulate land change.

Under the single-flip dynamics, each dynamic step involves an attempt to change the value of a randomly selected cell to its opposite value, essentially flipping it. The success or failure of this attempt depends on the flip probability, which is given by

$$P(x_k \to -x_k) = \frac{1}{1 + e^{\Delta E_k}}, \tag{2.2}$$

where ΔE_k is

$$\Delta E_k = (E_k^{\mathrm{af}} - E_k^{\mathrm{bf}}) + Q. \tag{2.3}$$

In equations (2.2) and (2.3) the quantity E_k is a contribution of cell k to $E(\omega_s)$. We have ommitted subscript s in the symbol for the local energy to make equation (2.3) more readable. The superscripts 'af' and 'bf' indicate 'before attempted flip' and 'after attempted flip', respectively. The probability of a flip is 0.5 when $\Delta E_k = 0$, it is high when $\Delta E_k < 0$, and it is low when $\Delta E_k > 0$.

In equation (2.3), the first term on the right-hand side represents the difference between the values of E_k associated with cell k after and before the attempted flip. The second term, denoted as Q, is not part of the Glauber dynamics or the original IM. It represents our modification of the algorithm aimed at reducing the occurrence of salt-and-pepper noise in the focus category when simulating the evolution of a coarse-textured pattern.

The value of Q is zero except in cases where cell k is equal to −1 (representing the background category) and all its neighbouring cells are also equal to −1. In such cases, with $Q = 0$, the probability of the cell flipping and becoming a focus cell is small but not small enough to prevent the generation of very small patches of the focus category, which is not observed in reality. By setting $Q \gg 0$, this probability becomes negligible, effectively eliminating the generation of small patches and eliminating the salt-and-pepper noise in the focus category.

For a cell with $Q = 0$, the change in energy ΔE_k is determined by the values of the cell k before and after an attempted flip, the sum S_k of values assigned to four cells neighbouring the focus cell, and the parameters J and B:

$$\Delta E_k = -(x_k^{\mathrm{af}} - x_k^{\mathrm{bf}})(JS_k + B). \tag{2.4}$$

The quantity S_k can take five possible values: −4, −2, 0, 2 and 4. On the other hand, the quantity $-(x_k^{\mathrm{af}} - x_k^{\mathrm{bf}})$ has three possible values: 2, 0 and −2, where the value of 0 corresponds to no flip.

Figure 1 illustrates 10 possible types of neighbourhoods in the IM. Each neighbourhood's centre cell has a high probability of flipping if the condition below the neighbourhood is true. For the centre

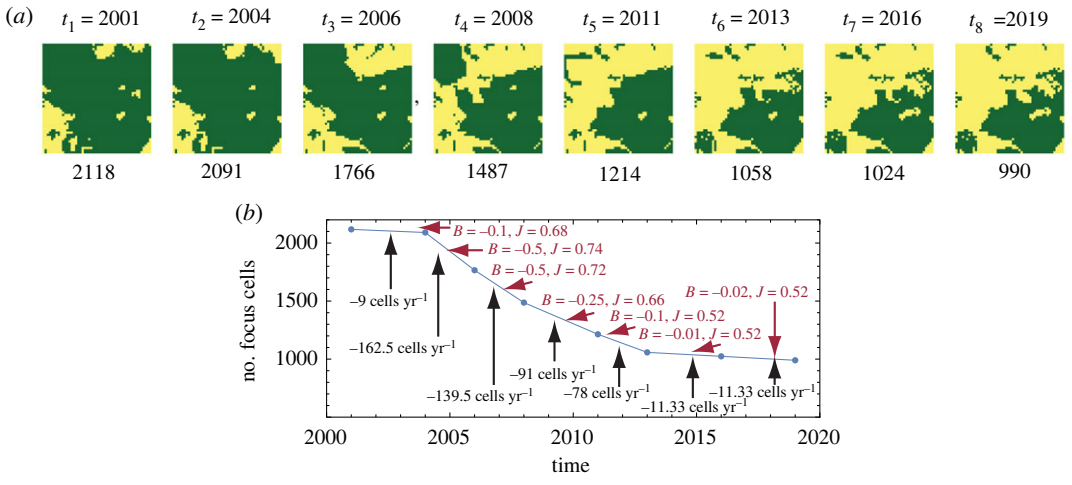

Figure 2. (*a*) The observed evolution of the land cover pattern from 2001 to 2019 is depicted for a small site measuring 1.5 km × 1.5 km, equivalent to 2500 cells. The focus category in this case is forest, and the observed process is deforestation. The numbers below the patterns indicate the count of focus cells. (*b*) A graph is presented to illustrate the temporal loss of focus (forest) cover during the seven transitions. The black descriptors represent the observed loss rates in cells per year, while the red descriptors represent the calculated values of the best-fit parameters for the simulated process.

neighbourhood in each row and in the absence of pressure to autocorrelate ($S_k = 0$), a high flip probability requires a small external push (B) towards the opposite category of the central cell. For the two left-most neighbourhoods in the top row, the flip probabilities can be high even in the presence of an external push in favour of the green category (positive B), as long as B has a sufficiently low absolute value. On the other hand, in the two right-most neighbourhoods in the top row, the flip probability can be high only if there is an external push in favour of the yellow category (negative B) with a high enough absolute value. The discussion of the bottom row in figure 1 is analogous.

2.1. Time unit

We aim to simulate a land change in a way depicted in figure 2*a*. The small, illustrative site shown in figure 2*a* undergoes deforestation, and it has been observed and mapped at eight different time instances. The time intervals between consecutive observations, denoted as $(\Delta t)_i$, where $i = 1, \ldots, 7$, are not constant. At each time interval, the area covered by the focus category (green) decreases. However, it is important to note that the rate of this decrease is not constant, as illustrated in figure 2*b*.

Our objective is to simulate the observed time series of patterns using the IM, with a focus on determining the optimal values for the IM parameters (B and J) for each transition in the series. In other words, we aim to find the best-fit values of B and J that result in the most accurate simulation of pattern changes during each time period $(\Delta t)_i$. In figure 2*b*, these best-fit parameter values are indicated in red. To obtain these values, we initiate the IM simulation with the observed pattern at time t_i (serving as the initial condition) and perform a series of Glauber dynamic steps corresponding to $(\Delta t)_i$. The goal is to generate a simulated pattern at t_{i+1} that closely resembles the observed pattern at that time.

To ensure that the number of dynamic steps taken is proportional to $(\Delta t)_i$, it is necessary to establish a unit of time that corresponds to the duration of a dynamic step. For instance, in the case of simulating the transition from 2001 to 2004 (as depicted in figure 2*a*), if we use 30 000 dynamic steps, we can set the time unit of a single dynamic step to 3 years divided by 30 000, which equals 0.876 h. This time unit can be interpreted as follows: in the landscape represented in figure 2*a*, a random cell within the array has an opportunity to change its land cover category every 0.876 h. The magnitude of this opportunity depends on the parameters of the IM model and the current landscape pattern.

Importantly, using a specific time for the dynamic step allows us to determine the number of steps required during the simulation of each transition. For the consecutive transitions shown in figure 2*a* the number of steps is 30 000, 20 000, 20 000, 30 000, 20 000, 30 000 and 30 000. A different time unit can be either larger or smaller than 0.876 h, but it must remain consistent throughout the simulation to ensure that the number of steps for each transition is proportional to its duration.

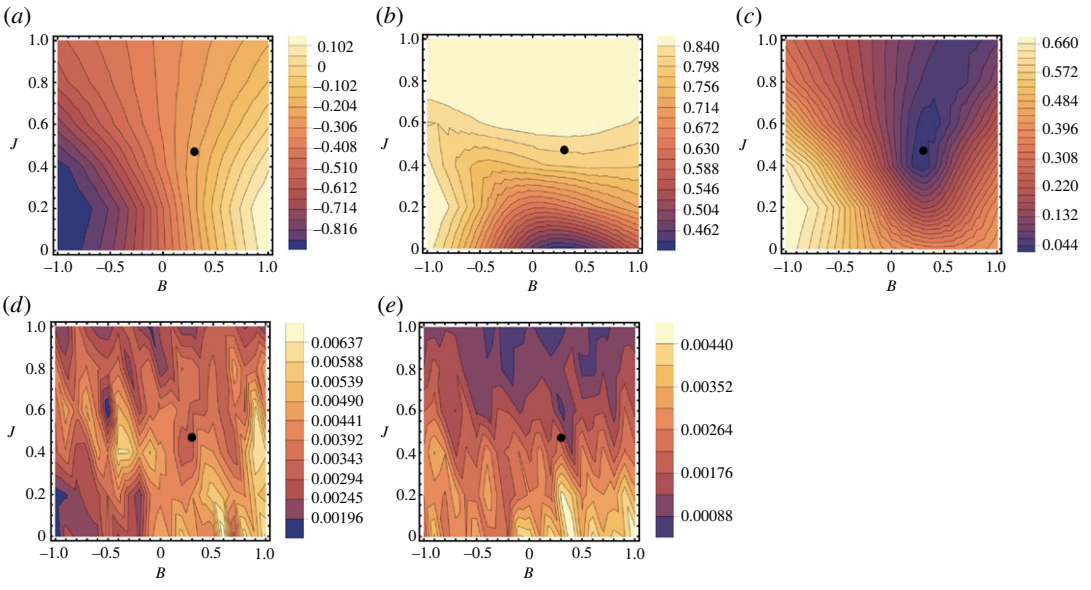

Figure 3. Functional dependencies of various parameters on the values of B and J during the 2008–2011 transition at the Iowa site. Panel (*a*) illustrates the behaviour of m_{sim}, while panel (*b*) depicts $\langle x_k\, x_{\ell'}\rangle_{\text{sim}}$. Panel (*c*) showcases the Euclidean distance between $(m, \langle x_k\, x_{\ell'}\rangle)_{\text{obs}}$ and $(m, \langle x_k\, x_{\ell'}\rangle)_{\text{sim}}$, providing insight into the goodness of fit. Panel (*d*) presents the standard deviation of m_{sim}, while panel (*e*) focuses on the standard deviations of $\langle x_k\, x_{\ell'}\rangle_{\text{sim}}$. The marked point denotes the optimal values of B and J, representing the best-fit solution.

2.2. Simulation

The simulation is performed on a transition-by-transition basis. Let us consider a specific transition from time t_1 to time t_2 with a duration of $(\Delta t)_1$ years. In our simulation of the four analysed sites (the next section), we employ n dynamic steps per year, where n represents the number of cells in the array. Theoretically, this means that each cell has the opportunity to undergo a flip once per year. Note that the time unit we use in our simulations is much smaller than 0.876 h used in an illustrative example shown in figure 2. This is because arrays we simulate have an order of magnitude more cells than arrays in the illustrative example.

The similarity between the observed and simulated patterns at time t_{i+1} is quantified using the Euclidean distance between pairs of indices encapsulating the observed $(m, \langle x_k\, x_{\ell'}\rangle)_{\text{obs}}$ and simulated $(m, \langle x_k\, x_{\ell'}\rangle)_{\text{sim}}$ patterns, respectively. Here, m represents the composition imbalance index of the landscape, which is calculated as $m = 2f - 1$, where f is the fraction of focus cells in the site. The range of m lies between -1 (indicating only background cells) and 1 (indicating only focus cells).

Additionally, $\langle x_k\, x_{\ell'}\rangle$ is a measure of the landscape's spatial autocorrelation, referred to as the texture index. It ranges from 0 (indicating fine texture) to 1 (indicating coarse texture). Computationally, $\langle x_k\, x_{\ell'}\rangle = C(1)$ is the lag one correlation function and $\langle \cdots \rangle$ denotes the ensemble average. Our objective is to determine the values of B and J that yield the highest similarity between the observed pattern at t_i and the simulated pattern at t_{i+1}, while considering the constraints of the number of dynamic steps (proportional to $(\Delta t)_i$) and periodic boundary conditions.

The best-fit values of B and J are determined using the simulated annealing optimization algorithm [50]. We employ the implementation of this algorithm provided by the optimization package in R [51]. A detailed example of the optimization workflow can be found in the vignette of the spatializing R package [52].

Since the Glauber dynamics is stochastic in nature, we repeat the aforementioned procedure 200 times to obtain an ensemble of best-fit parameter pairs (B and J). From this ensemble, we select the pair that corresponds to the peak of the frequency distribution of pairs. This chosen pair represents our final solution for the parameters, characterizing the magnitude and nature of the process governing the pattern change during the transition from t_i to t_{i+1}. The same procedure is applied to determine the solutions for the remaining transitions.

Figure 3*a*,*b* depicts the functional dependencies of m_{sim} and $\langle x_k\, x_{\ell'}\rangle_{\text{sim}}$ on the values of parameters B and J to show how the changes of these values influence the character of simulated pattern. This particular figure corresponds to the 2008–2011 transition at the Iowa site (as detailed in table 1), but it serves as a representative example for all transitions across various sites. Contour plots illustrate the

Table 1. Best-fit process parameters.

process	coordinates	2001 → 2004	2004 → 2006	2006 → 2008	2008 → 2011	2011 → 2013	2013 → 2016	2016 → 2019
reforestation	69.31298 W	$B = 0.18$	$B = 0.48$	$B = 0.76$	$B = 0.05$	$B = 0.09$	$B = 0.095$	$B = 0.06$
Maine	46.65407 N	$J = 0.42$	$J = 0.40$	$J = 0.38$	$J = 0.45$	$J = 0.45$	$J = 0.45$	$J = 0.45$
croplands gain	93.28743 W	$B = 0.16$	$B = 0.25$	$B = 0.22$	$B = 0.28$	$B = 0.15$	$B = 0.07$	$B = -0.001$
Iowa	40.86183 N	$J = 0.50$	$J = 0.50$	$J = 0.50$	$J = 0.45$	$J = 0.50$	$J = 0.50$	$J = 0.55$
wetland loss	81.85418 W	$B = 0.04$	$B = -0.06$	$B = -0.03$	$B = -0.12$	$B = -0.05$	$B = -0.03$	$B = -0.045$
Florida	26.86219 N	J = 0.34	$J = 0.32$	$J = 0.32$	$J = 0.33$	$J = 0.33$	$J = 0.34$	$J = 0.35$
open-pit mining	105.28693 W	$B = 0.15$	$B = 0.8$	$B = 0.4$	$B = 0.47$	$B = -0.03$	$B = 0.732$	$B = 0.28$
Wyoming	43.69249 N	$J = 0.50$	$J = 0.50$	$J = 0.50$	$J = 0.50$	$J = 0.60$	$J = 0.60$	$J = 0.50$

functions $m_{\mathrm{sim}}(B, J)$ and $\langle x_k\, x_\ell\rangle_{\mathrm{sim}}(B, J)$, with colors indicating the values of these functions. The most significant observation is that the behaviour of m_{sim} exhibits heightened sensitivity to changes in the parameter B, while $\langle x_k\, x_\ell\rangle_{\mathrm{sim}}$ is primarily influenced by variations in the parameter J. It is worth noting that, beyond a certain threshold value of J (approx. 0.6 in this example), $\langle x_k\, x_\ell\rangle_{\mathrm{sim}}$ ceases to be significantly affected by either B or J.

In figure 3*c*, we explore the functional relationship characterizing the fitting criterion, which is defined as the Euclidean distance between $(m, \langle x_k\, x_\ell\rangle)_{\mathrm{obs}}$ and $(m, \langle x_k\, x_\ell\rangle)_{\mathrm{sim}}$. This function exhibits a single minimum, representing the optimal fit solution. Notably, good fits can also be achieved by employing an optimal value of B in conjunction with values of J that surpass the optimal J value. The presence of single minimum holds true across all transitions and sites investigated in our study. The region of a good fit around the minimum is narrowly constrained by B in all cases, in some instances, it is also more narrowly constrained by J than in the case depicted in figure 3.

Finally, figure 3*d*,*e* illustrates the functional dependencies of the standard deviations pertaining to m_{sim} and $\langle x_k\, x_\ell\rangle_{\mathrm{sim}}$ around their respective ensemble averages, with respect to the parameters B and J. Notably, in all instances, these standard deviations are very small. This result implies that each simulated instance of the pattern has, with good approximation, the same area and texture.

3. Results

To assess the feasibility of the IM to simulate the land change, we conducted calculations for four sites. The sites were selected to exhibit different processes leading to the change of pattern with time: reforestation, expansion of croplands, wetland loss and open-pit mining. The observed change is documented by the NLCD2019 dataset that shows LULC maps of those sites at eight different times starting in 2001 and ending in 2019. Each site is represented by a time series of eight arrays of $n = 250 \times 250 = 62\,500$ LULC-labelled cells. Calculations are conducted using a protocol as described in §2.

Best-fit values of parameters B and J for each transition are shown in table 1. The simulated land's pattern is compared to an observed land's pattern in multiple ways. First, we compare values of m (expressed in terms of the number of focus cells) and $\langle x_k\, x_\ell\rangle$ in simulated and observed land patterns. The similarity of these values indicates a similarity in the area and texture of the focus cells' observed and simulated patterns.

Second, we compare mapped and simulated complementary cumulative distribution functions (cCDF) of patch size and area. Patches are sets of adjacent cells of focus category; they are extracted using the connected components labelling algorithm [53]. The cCDF is the probability that the variable takes a value greater than a pre-specified value. For example, in the case of the patch size distribution, cCDF(10) = 0.1 means that 10% of patches have sizes larger than 10 cells. In the case of the area distribution, cCDF(10) = 0.9 means that 90% of the area covered by the focus category is in patches having a size larger than 10 cells.

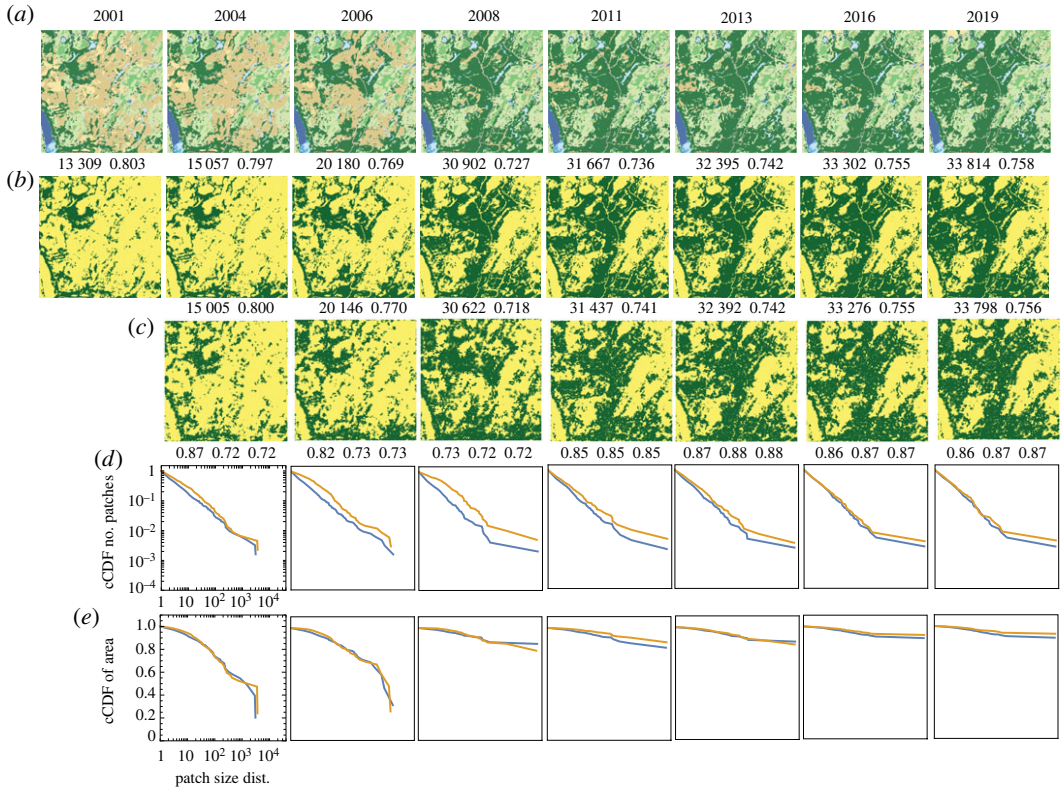

Figure 4. Comparison between the observed and the simulated land change at a site in the US state of Maine undergoing the reforestation process during the 2001–2019 period. (*a*) The series of original NLCD2019 maps of LULC categories. (*b*) NLCD2019 maps reclassified into two categories, the focus category (evergreen forest) and the background. (*c*) Simulated land change. (*d*) Complementary CDFs of patch size for the patterns in (*b*) (blue) and (*c*) (orange). (*e*) Complementary CDFs of patch area for the patterns in (*b*) (blue) and (*c*) (orange). The numbers above observed and simulated patterns are the number of forest cells and the pattern's texture parameter $\langle x_k\ x_\ell \rangle$. Numbers below the simulated patterns are accuracy, recall and precision.

Third, we treat simulation as a prediction and calculate prediction metrics, accuracy, recall (for the focus category) and precision (for the focus category). A recall is the estimated probability that a cell randomly selected from among focus cells in the observed landscape is also a focus cell in the simulated landscape. Precision is the estimated probability that a cell randomly selected from among focus cells in the simulated pattern is also a focus cell in the observed pattern. High values of recall and precision indicate individual cell-level agreement between two patterns. Top empirical models achieve values of recall and precision of approximately 90% (e.g. [54]).

3.1. Reforestation

Our first site is located in Aroostook county in northern Maine. This county has a notable historical trend of deforestation; however, a significant shift has occurred in the forest condition since approximately 2005 [55]. The selected site serves as an illustrative example of this turnaround. The results obtained for this site are presented in figure 4, which consists of five rows.

In the first row of figure 4, NLCD2019 maps of the site from 2001 to 2019 are displayed, where different colours represent distinct LULC categories. The second row exhibits the same NLCD2019 maps, but this time they are reclassified into binary patterns. In these reclassified patterns, the focus category is represented by dark green colour, corresponding to the evergreen forest category (category 42 in the NLCD2019 maps), as depicted in the first row of the figure.

The third row of figure 4 displays the results of our simulations, using the best-fit values of B and J for each transition (listed in the first entry of table 1). Upon visual inspection, the observed time series (figure 4*b*) and the simulated time series (figure 4*c*) exhibit a striking similarity. However, upon closer examination, some discrepancies can be observed, particularly during the period of the most significant change, $(\Delta t)_2$ and $(\Delta t)_3$. Quantitatively, both the observed and simulated time series are characterized by nearly identical values of m and $\langle x_k\ x_\ell \rangle$, indicating a high degree of similarity in

terms of composition and texture. The recall and precision values are approximately 70% from 2004 to 2008, corresponding to a period of rapid change, and approximately 90% from 2011 to 2019, during a period of slower change.

The fourth row of figure 4 illustrates the patch size distributions for both the observed patterns (blue) and the simulated patterns (orange). Overall, the patch size distributions of the observed and simulated patterns exhibit a high degree of similarity. Any differences observed in the size distributions primarily arise from variations in the size and/or number of the largest patches. These differences may not be apparent when examining the patterns themselves since the distinction between a single large patch and multiple smaller patches may depend on the presence or the absence of a single cell that connects the larger patches.

The fifth row presents the area distributions for the observed patterns (blue) and the simulated patterns (orange). The area distributions of both the observed and simulated patterns demonstrate remarkable similarity. It is noteworthy that as time progresses, a significant majority of focus cells aggregate into a single, very large patch. This indicates that the initially fragmented forest gradually reconnects, forming a cohesive and connected forest structure.

The values of B exhibit temporal variability throughout the period from 2001 to 2019 (table 1). This variability is strongly correlated with the fluctuation of the reforestation rate, as indicated by a correlation coefficient of 0.99. This finding suggests that an external force is responsible for driving the temporal changes in the reforestation rate. On the other hand, the values of J remain relatively constant over the entire 2001–2019 period, with an approximate value of $J \approx 0.4$. This suggests that the propensity of the land to exhibit spatial autocorrelation remained consistent throughout the studied period. However, the specific mechanisms underlying the external influence and the tendency for autocorrelation are beyond the scope of this paper and will require further investigation.

3.2. Expansion of croplands

The expansion of croplands in the USA is causing a decline in grasslands and other ecosystems. One of the regions experiencing significant expansion is southern Iowa, as documented by Lark *et al.* [56]. Our second site, located at the boundary between Lucas and Wayne counties in Iowa, serves as an illustrative example of this expansion. The results for this site are presented in figure 5. The figure follows the same organization as figure 4, with the green colour in the second and third rows indicating cultivated crops (NLCD category 82), represented by a brown colour in the first row.

The second row in table 1 presents the best-fit values of B and J for each transition in the series depicted in figure 5. Similar to the reforestation site discussed in §3.1, we observe a high visual similarity between the simulated and observed series. However, there is a notable difference in the presence of grid-like north–south and east–north features in the observed patterns that are absent in the simulated patterns. These features can be attributed to a historical system dating back to the early days of the USA, where land was divided into one-square-mile quadrangles where feasible. While the IM cannot replicate these grid-like features, it accurately reproduces the overall changing arrangement of croplands in this site.

The quantitative analysis reveals that the simulated and observed patterns exhibit almost identical values of m and $\langle x_k\ x_\ell \rangle$. It is important to recall that our criterion for determining the best-fit values of B and J relies on the similarity between the simulated and observed values of m and $\langle x_k\ x_\ell \rangle$, which serves as the fitness function. The excellent fit obtained indicates that the IM can be effectively tailored to the data. Additionally, the recall and precision values are approximately 70% from 2004 to 2008 (during periods of rapid change) and around 90% from 2011 to 2019 (during periods of slower change). These recall and precision values are comparable to those achieved by empirical models of land change, indicating the effectiveness of the IM in capturing the dynamics of the studied site.

Figure 5*d* illustrates the patch size distributions for the observed patterns (blue) and simulated patterns (orange). It is important to note that the y-axis represents the probability that a randomly selected patch has a size equal to or larger than the corresponding value on the x-axis. Upon examining the series of distributions in figure 5*d*, we can observe that the observed land patterns exhibit a relatively higher frequency of smaller patches and a relatively lower frequency of larger patches compared to the simulated patterns. This finding is further supported by figure 5*e*. Despite the high values of recall and precision, the discrepancies observed in the size and area distributions can be attributed to the IM's inability to reproduce the linear background features mentioned earlier, which exist in the observed land and contribute to the division of the area into smaller patches.

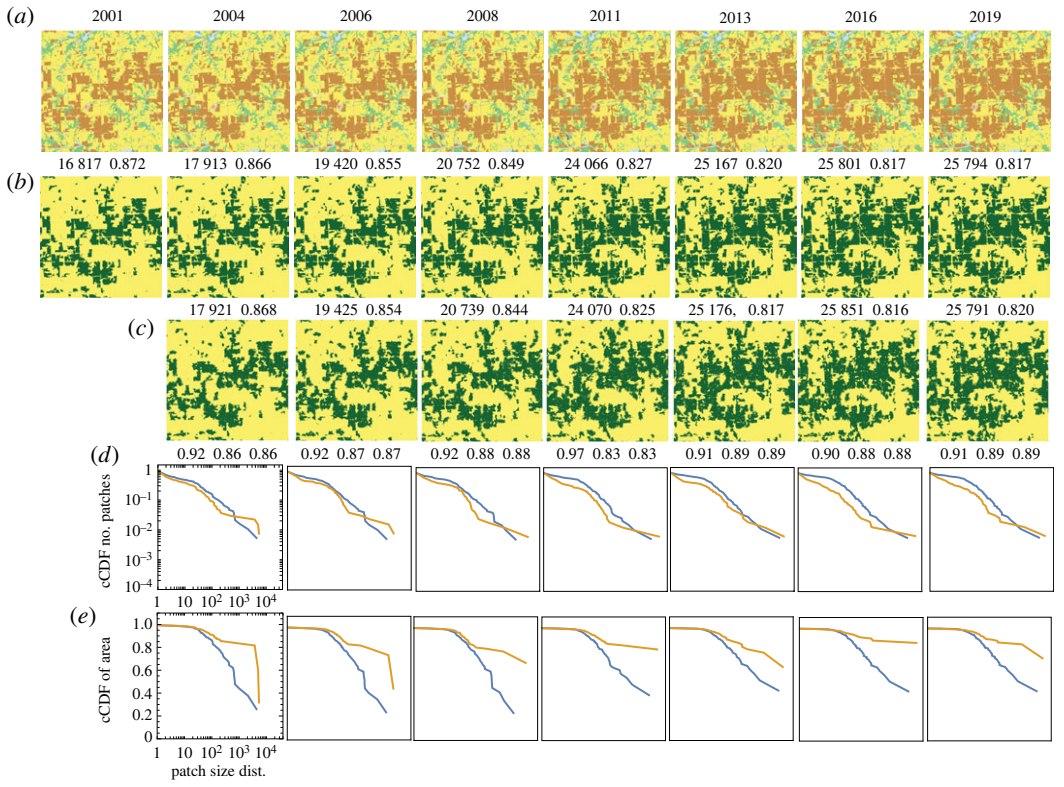

Figure 5. Comparison of the observed and the simulated land change at a site in the US state of Iowa undergoing a crop expansion process during the 2001–2019 period. (*a*) The series of original NLCD2019 maps of LULC categories. (*b*) NLCD2019 maps reclassified into two categories, the focus category (crops) and the background. (*c*) Simulated land change. (*d*) Complementary CDFs of patch size for the patterns in (*b*) (blue) and (*c*) (orange). (*e*) Complementary CDFs of patch area for the patterns in (*b*) (blue) and (*c*) (orange). The numbers above observed and simulated patterns are the number of cropland cells and the pattern's texture parameter $\langle x_k\, x_\ell \rangle$. Numbers below the simulated patterns are accuracy, recall and precision.

Similar to the deforestation example discussed in §3.1, the cropland expansion case also exhibits a strong correlation (0.87) between the inferred values of B and the rate of cropland gain. On the other hand, the inferred values of J remain relatively constant throughout the 2001–2019 period. This observation leads to a hypothesis that external influences, potentially of an economic nature [56], are responsible for the temporal changes in cropland expansion, while the autocorrelation tendency is an inherent characteristic of the site that remains unchanged over the observed time period.

3.3. Loss of herbaceous wetlands

Our third site is situated within the Fred C. Babcock/Cecil M. Webb Wildlife Management Area (WMA) in southwestern Florida. This particular site is predominantly composed of two types of wetlands: woody wetlands (NLCD category 90, depicted in a lighter blue shade in figure 6*a*) and herbaceous wetlands (NLCD category 95, depicted in a darker blue shade in figure 6*a*). Our focus category for analysis is the herbaceous wetlands, which exhibits distinct patterns compared to the previous examples, characterized by a finer-grained structure.

The third row in table 1 presents the best-fit values of B and J for each transition in the series depicted in figure 6. Notably, the values of B are negative, indicating a decrease in the area of the focus category. The values of J remain relatively constant for the duration of the observed period, but they are smaller compared to the previous two sites, suggesting a lower inherent tendency for spatial autocorrelation. This observation aligns with the fine-grained nature of the landscape pattern observed in this particular site.

Similar to the previous two examples, we observe a strong visual resemblance between the simulated and observed land series in this case. However, it is important to note that visual assessment may not be entirely reliable due to the limited spatial variability in the wetlands patterns at this small scale. To obtain a more accurate evaluation, we rely on quantitative measures. Quantitatively, the simulated and observed

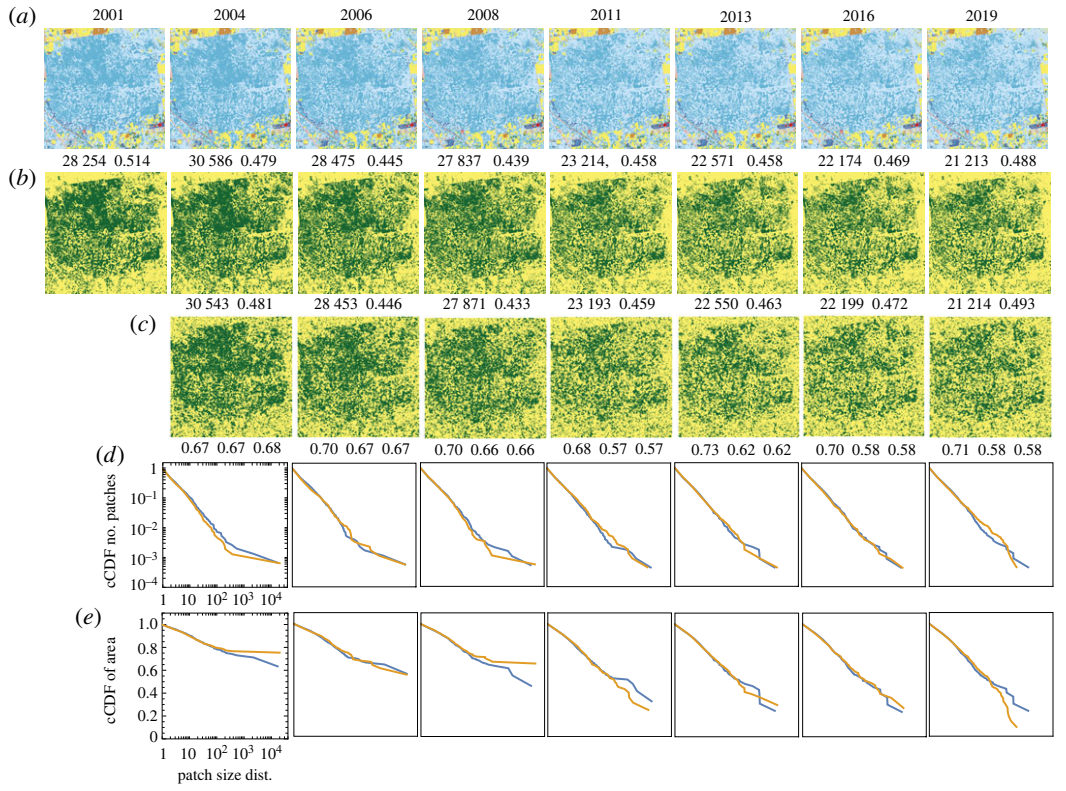

Figure 6. Comparison of the observed and the simulated land change at a site in the US state of Florida undergoing a herbaceous wetlands loss process during the 2001–2019 period. (*a*) The series of original NLCD2019 maps of LULC categories. (*b*) NLCD2019 maps reclassified into two categories, the focus category (herbaceous wetlands) and the background. (*c*) Simulated evolution of land change. (*d*) Complementary CDFs of patch size for the patterns in (*b*) (blue) and (*c*) (orange). (*e*) Complementary CDFs of patch area for the patterns in (*b*) (blue) and (*c*) (orange). The numbers above observed and simulated patterns are the number of herbaceous wetland cells and the pattern's texture parameter $\langle x_k\, x_\ell \rangle$. Numbers below the simulated patterns are accuracy, recall and precision.

patterns exhibit nearly identical values of m and $\langle x_k\, x_\ell \rangle$, indicating that the IM can effectively capture and reproduce this type of pattern as well.

The values of recall and precision in this case are in the range of 70–60%, which is lower compared to the previous two examples. We attribute this lower cell-level accuracy to the fine-grained nature of the wetlands pattern. The stochasticity of the Glauber dynamics in the IM leads to distinct realizations of the simulation at the cell level, resulting in differences between individual patterns. This variability is more pronounced in fine-grained patterns, leading to a decrease in accuracy. However, it is worth noting that despite the lower cell-level accuracy, the distributions of patch sizes and areas in both the observed and simulated patterns exhibit a high degree of similarity, as the majority of patches in this landscape are small.

The loss of herbaceous wetlands exhibits a high correlation (0.99) with the inferred values of parameter B. This finding aligns with our previous examples and reinforces our conclusion that parameter B governs the temporal variability of landscape composition. In this specific case, it influences the loss of herbaceous wetlands. On the other hand, parameter J remains consistent and does not undergo significant changes over the observed time scale, highlighting its role as a property inherent to the site.

3.4. Open-pit mining

The fourth site encompasses the Black Thunder Coal Mine located in Wyoming. This site is characterized by an open-pit mine, where the landscape predominantly consists of barren land (NLCD category 31), depicted by a grey colour in the NLCD maps shown in figure 7. Additionally, the site includes grassland (NLCD category 71) depicted by a vanilla colour, and shrubland (NLCD category 52) depicted by a beige colour. The focus category in this case is the barren land, which corresponds to

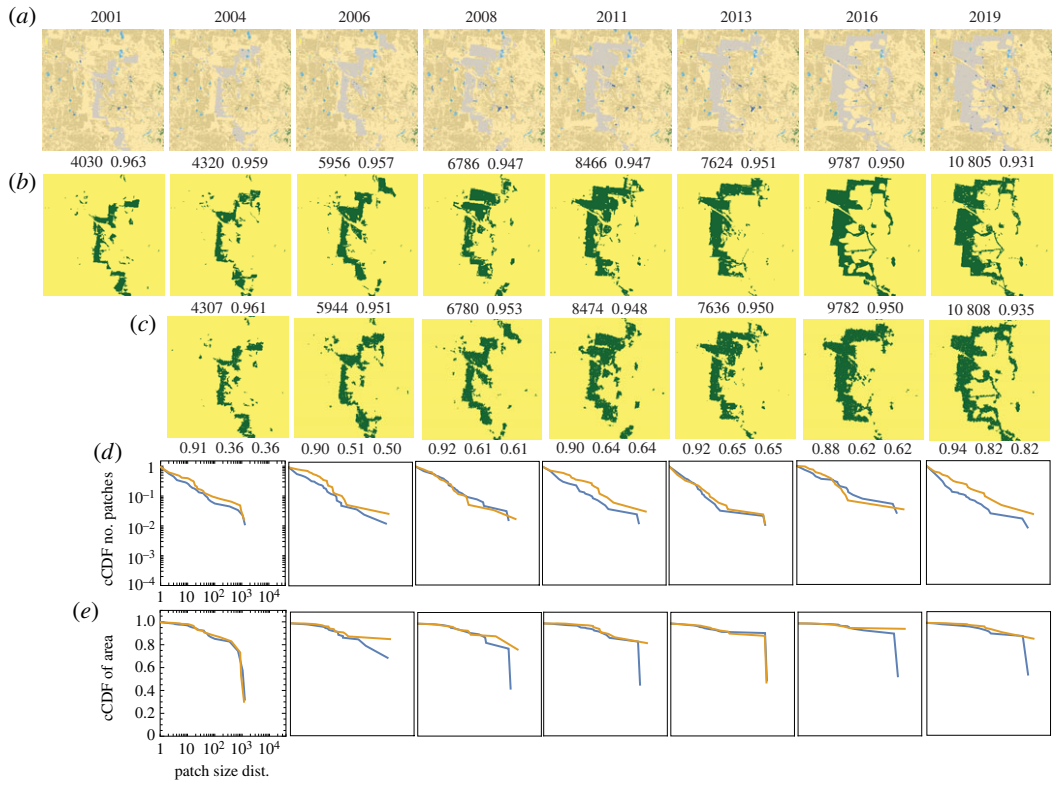

Figure 7. Comparison of the observed and the simulated land change at a site in the US state of Wyoming undergoing a change due to mining activity during the 2001–2019 period. (*a*) The series of original NLCD2019 maps of LULC categories. (*b*) NLCD2019 maps reclassified into two categories, the focus category (barren land) and the background. (*c*) Simulated evolution of the site. (*d*) Complementary CDFs of patch size for the patterns in (*b*) (blue) and (*c*) (orange). (*e*) Complementary CDFs of patch area for the patterns in (*b*) (blue) and (*c*) (orange). The numbers above observed and simulated patterns are the number of barren land cells and the pattern's texture parameter $\langle x_k\, x_{\ell'} \rangle$. Numbers below the simulated patterns are accuracy, recall and precision.

the pit within the mine. Notably, the pattern evolution in this site deviates from the previous examples, as the pit has undergone a westward shift during the 2001–2019 period.

The fourth row in table 1 presents the best-fit values of B and J for each transition in the series depicted in figure 7. Notably, the values of B exhibit significant variability from one observation year to another, indicating an uneven external influence. One plausible explanation for this variability is the fluctuating demand for coal. Conversely, the values of J remain relatively constant during the observed period. Similarly to the previous examples, we observe a high visual similarity between the simulated and observed land series. Furthermore, a quantitative analysis reveals that the simulated and observed patterns are characterized by nearly identical values of m and $\langle x_k\, x_{\ell'} \rangle$.

The values of recall and precision exhibit variability, ranging from 36% to 51% for the first two transitions, approximately 60% for the subsequent four transitions, and 82% in the final transition. These values display an inverse correlation with the rate at which the pit shifts westward, with lower accuracy observed during faster shifts and higher accuracy during slower shifts. This outcome can be attributed to the limitations of the IM, which lacks a preferred direction in its dynamics and therefore cannot shift the pattern of focus cells from their initial position. The discrepancies observed in the shapes of patch size and area distributions are primarily attributed to the model's inability to form linear features, as discussed in the previous subsections.

4. Discussion

Our hypothesis in the Introduction suggested that the kinetic IM can serve as a framework for understanding various land change processes. By employing a bare-bones change model, we can abstract the underlying dynamics of change from the specific real-world processes associated with thematic contexts and locations of different sites. Furthermore, this model allows us to quantify

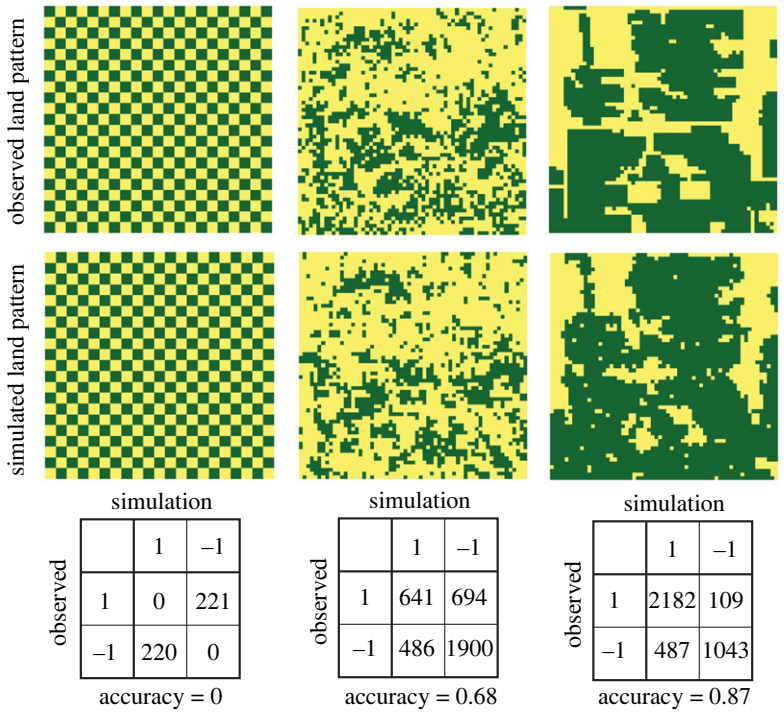

Figure 8. Comparison between observed and simulated patterns, along with their respective confusion matrices. (Left) A synthetic land pattern exhibits a discrepancy from the observation due to a one-cell shift. Although the two patterns are essentially identical, the accuracy inferred from the confusion matrix is recorded as 0. (Middle) A fragment of the 2011 land pattern, as depicted in figure 6. In this case, the observed and simulated patterns share the same character. However, owing to the stochastic nature of the IM a good cell-level match of categories is not attainable, resulting in an accuracy score of 0.68. (Right) A fragment of the 2011 land pattern, as displayed in figure 5. The observed and simulated patterns clearly possess the same character. Furthermore, due to the coarse texture of this particular pattern, the stochastic nature of the simulation does not significantly impact the cell-level match of categories, resulting in a higher accuracy score of 0.87.

change not only in terms of the extent of the altered area but also in terms of the intensity of the process. We now examine whether our results support the hypothesis that the IM can effectively serve as an abstraction of land change processes. The summary of our evaluation is as follows:

1. *Visual similarity:* We observed a high degree of visual similarity between the simulated and observed land series in all four case studies, indicating that the IM captures the overall patterns and dynamics of land change accurately.
2. *Quantitative measures:* The simulated and observed patterns exhibited nearly identical values of key quantitative pattern measures, such as the composition imbalance index m and the texture index $\langle x_k\ x_\epsilon \rangle$. Patch size distribution in simulated and observed patterns also match except for the largest patches. This shows that the IM can effectively reproduce temporal changes in the composition and texture of landscape pattern.
3. *Parameter correlations:* We found strong correlations between inferred values of parameter B and rate of change. This indicates that the IM successfully captures the temporal variability of landscape composition in response to changing external forces.
4. *Model limitations:* There are some discrepancies between modelled and observed land change. The IM could not reproduce linear features, pattern shifts, and formation of large new patches.

Our findings provide compelling evidence that the fundamental principles of the IM, external influences and internal coupling between neighbouring cells, are crucial factors driving various observed land change phenomena. This insight constitutes the primary original contribution of our research. By successfully demonstrating the IM's capability to accurately capture the dynamics of land change across different thematic contexts and locations, we highlight that the specific intricacies of these underlying mechanisms may not be the determining factors in shaping the magnitude and nature of change. Instead, it is the interplay between external forcing and short-range interactions, regardless of their origin, that drives the observed patterns of change in land.

As mentioned in the Introduction, the aim of this work was not to apply the IM for land change prediction. However, our analysis of the four examples has demonstrated that the IM has the capability to predict the spatial arrangement of future patterns given the initial conditions, the future bulk composition, and an assumed constant value of J. The requirement of knowing the future bulk composition is common to all spatially explicit models, including empirical, mechanistic, and agent-based models, as they rely on understanding the extent of change (referred to as a scenario; e.g. Zhou *et al*. [57]) in order to make predictions about future spatial patterns. As a cell-level predictor, the IM has shown reasonable accuracy for predicting reforestation and crop expansion sites, but lower accuracy for wetlands and mining sites. It is important to note that the accuracy of empirical predictors on wetlands and mining sites is also unclear, as these sites pose unique challenges for modelling.

In land science, the evaluation of simulation accuracy is conventionally carried out through the utilization of a confusion matrix. In our context, the confusion matrix takes the form of a 2×2 contingency table, where the rows correspond to the actual categories, and the columns represent the categories as predicted by a simulation. The values of accuracy, recall and precision, as presented in figures 4 to 7, are derived from these confusion matrices. However, such assessment method may not be ideally suited for gauging the accuracy of a stochastic model, whose primary function is to forecast the characteristics of a pattern (values of indices m and $\langle x_k\ x_c \rangle$, and the value of an index of the patch-size distribution). In our simulations, the accuracy values may fall within a spectrum ranging from good to reasonable. Nonetheless, even if these values were to be lower, it would not necessarily signify a failure, as long as the aforementioned indices are effectively matched. The rationale behind this assertion is elucidated in figure 8.

Finally, it is important to emphasize that our utilization of the IM deviates from its conventional application. While the classic IM is traditionally employed to deduce equilibrium land patterns based on prescribed values of B and J or to ascertain the values of B and J associated with the first-order phase transitions [35], our study repurposed the IM as a tool for simulating land-use changes. This approach introduces a novel application for the well-established IM, expanding its utility to the realm of land change modelling.

Ethics. This work did not require ethical approval from a human subject or animal welfare committee.

Data accessibility. This article has no additional data.

Declaration of AI use. We have not used AI-assisted technologies in creating this article.

Authors' contributions. T.F.S.: conceptualization, formal analysis, methodology, writing—original draft; J.N.: software, validation, writing—review and editing.

All authors gave final approval for publication and agreed to be held accountable for the work performed therein.

Conflict of interest declaration. We declare we have no competing interests.

Funding. No funding has been received for this article.

References

1. Winkler K, Fuchs R, Rounsevell M, Herold M. 2021 Global land use changes are four times greater than previously estimated. *Nat. Commun.* **12**, 2501. (doi:10.1038/s41467-021-22702-2)
2. Song X-P, Hansen MC, Stehman SV, Potapov PV, Tyukavina A, Vermote EF, Townshend JR. 2018 Global land change from 1982 to 2016. *Nature* **560**, 639–643. (doi:10.1038/s41586-018-0411-9)
3. Hansen MC *et al.* 2013 High-resolution global maps of 21st-century forest cover change. *Science* **342**, 850–853. (doi:10.1126/science.1244693)
4. Venter O *et al.* 2016 Sixteen years of change in the global terrestrial human footprint and implications for biodiversity conservation. *Nat. Commun.* **7**, 12558. (doi:10.1038/ncomms12558)
5. Li W, MacBean N, Ciais P, Defourny P, Lamarche C, Bontemps S, Houghton RA, Peng S. 2018 Gross and net land cover changes in the main plant functional types derived from the annual ESA CCI land cover maps (1992–2015). *Earth Syst. Sci. Data* **10**, 219–234. (doi:10.5194/essd-10-219-2018)
6. Nowosad J, Stepinski TF, Netzel P. 2019 Global assessment and mapping of changes in mesoscale landscapes: 1992–2015. *Int. J. Appl. Earth Obs. Geoinformation* **78**, 332–340. (doi:10.1016/j.jag.2018.09.013)
7. Liu T, Yang X. 2015 Land change modeling: status and challenges. In *Monitoring and modeling of global changes: a geomatics perspective* (eds J Li, X Yang), pp. 3–16. Dordrecht, The Netherlands: Springer. (doi:10.1007/978-94-017-9813-6_1)
8. Veldkamp A, Lambin EF. 2001 Predicting land-use change. *Agric. Ecosyst. Environ.* **85**, 1–6. (doi:10.1016/S0167-8809(01)00199-2)
9. Camacho Olmedo M, Mas J, Paegelow M. 2018 The simulation stage in LUCC modeling. In *Geomatic approaches for modeling land change scenarios* (eds M Camacho Olmedo, M Paegelow, J Mas, F Escobar), pp. 27–51. Cham, Switzerland: Springer. (doi:10.1007/978-3-319-60801-3_3)
10. Turner MG. 1989 Landscape ecology: the effect of pattern on process. *Annu. Rev. Ecol. Evol. Syst.* **20**, 171–197. (doi:10.1146/annurev.es.20.110189.001131)
11. Gustafson EJ. 2013 When relationships estimated in the past cannot be used to predict the future: using mechanistic models to predict landscape ecological dynamics in a changing world. *Landscape Ecol.* **28**, 1429–1437. (doi:10.1007/s10980-013-9927-4)
12. Rastetter EB, Aber JD, Peters DP, Ojima DS, Burke IC. 2003 Using mechanistic models to scale ecological processes across space and time. *BioScience* **53**, 68–76. (doi:10.1641/0006-3568(2003)053[0068:UMMTSE]2.0.CO;2)

13. Scheller RM, Domingo JB, Sturtevant BR, Williams J, Rudy A, Gustafson EJ, Mladenoff DJ. 2007 Design, development, and application of LANDIS-II, a spatial landscape simulation model with flexible temporal and spatial resolution. *Ecol. Modell.* **201**, 409–419. (doi:10.1016/j.ecolmodel.2006.10.009)
14. Valbuena D, Verburg PH, Bregt AK, Ligtenberg A. 2010 An agent-based approach to model land-use change at a regional scale. *Landscape Ecol.* **25**, 185–199. (doi:10.1007/s10980-009-9380-6)
15. Gardner RH, Milne BT, Turnei MG, O'Neill RV. 1987 Neutral models for the analysis of broad-scale landscape pattern. *Landscape Ecol.* **1**, 19–28. (doi:10.1007/BF02275262)
16. Gaucherel C, Houet T. 2009 Preface to the selected papers on spatially explicit landscape modelling: current practices and challenges. *Ecol. Modell.* **220**, 3477–3480. (doi:10.1016/j.ecolmodel.2009.06.025)
17. Gaucherel C, Houllier F, Auclair D, Houet T. 2014 Dynamic landscape modelling: the quest for a unifying theory. *Living Rev. Landscape Res.* **8**, 5–31. (doi:10.12942/lrlr-2014-2)
18. Brush SG. 1967 History of the Lenz-Ising model. *Rev. Mod. Phys.* **39**, 883–893. (doi:10.1103/RevModPhys.39.883)
19. Cipra BA. 1987 An introduction to the Ising model. *Am. Math. Mon.* **94**, 937–959. (doi:10.1080/00029890.1987.12000742)
20. Ising E. 1924 Beitrag zur theorie des ferro-und paramagnetismus. PhD thesis, Grefe & Tiedemann.
21. Onsager L. 1944 Crystal statistics. I. A two-dimensional model with an order-disorder transition. *Phys. Rev.* **65**, 117–149. (doi:10.1103/PhysRev.65.117)
22. Cihlar J. 2000 Land cover mapping of large areas from satellites: status and research priorities. *Int. J. Remote Sens.* **21**, 1093–1114. (doi:10.1080/014311600210092)
23. Bornholdt S, Wagner F. 2002 Stability of money: phase transitions in an Ising economy. *Physica A* **316**, 453–468. (doi:10.1016/S0378-4371(02)01218-9)
24. Stauffer D. 2008 Social applications of two-dimensional Ising models. *Am. J. Phys.* **76**, 470–473. (doi:10.1119/1.2779882)
25. Brandt MJ, Sleegers WW. 2021 Evaluating belief system networks as a theory of political belief system dynamics. *Pers. Soc. Psychol. Rev.* **25**, 159–185. (doi:10.1177/1088868321993751)
26. Cramer AO, Van Borkulo CD, Giltay EJ, Van Der Maas HL, Kendler KS, Scheffer M, Borsboom D. 2016 Major depression as a complex dynamic system. *PLoS ONE* **11**, e0167490. (doi:10.1371/journal.pone.0167490)
27. Majewski J, Li H, Ott J. 2001 The Ising model in physics and statistical genetics. *Am. J. Human Genet.* **69**, 853–862. (doi:10.1086/323419)
28. Ma Y-P, Sudakov I, Strong C, Golden KM. 2019 Ising model for melt ponds on Arctic sea ice. *New J. Phys.* **21**, 063029. (doi:10.1088/1367-2630/ab26db)
29. Katori M, Kizaki S, Terui Y, Kubo T. 1998 Forest dynamics with canopy gap expansion and stochastic Ising model. *Fractals* **6**, 81–86. (doi:10.1142/S0218348X98000092)
30. Kizaki S, Katori M. 1999 Analysis of canopy-gap structures of forests by Ising-Gibbs states-equilibrium and scaling property of real forests. *J. Phys. Soc. Jpn.* **68**, 2553–2560. (doi:10.1143/JPSJ.68.2553)
31. Schlicht R, Iwasa Y. 2006 Deviation from power law, spatial data of forest canopy gaps, and three lattice models. *Ecol. Modell.* **198**, 399–408. (doi:10.1016/j.ecolmodel.2006.05.013)
32. Scanlon TM, Caylor KK, Levin SA, Rodriguez-Iturbe I. 2007 Positive feedbacks promote power-law clustering of Kalahari vegetation. *Nature* **449**, 209–212. (doi:10.1038/nature06060)
33. Nareddy VR, Machta J, Abbott KC, Esmaeili S, Hastings A. 2020 Dynamical Ising model of spatially coupled ecological oscillators. *J. R. Soc. Interface* **17**, 20200571. (doi:10.1098/rsif.2020.0571)
34. Noble AE, Rosenstock TS, Brown PH, Machta J, Hastings A. 2018 Spatial patterns of tree yield explained by endogenous forces through a correspondence between the Ising model and ecology. *Proc. Natl Acad. Sci. USA* **115**, 1825–1830. (doi:10.1073/pnas.1618887115)
35. Stepinski TF. 2023 Spatially explicit simulation of deforestation using the Ising-like neutral model. *Environ. Res. Ecol.* **2**, 025003. (doi:10.1088/2752-664X/acdbd2)
36. Jamaludin J, Alban JDTD, Carrasco LR, Webb EL. 2022 Spatiotemporal analysis of deforestation patterns and drivers reveals emergent threats to tropical forest landscapes. *Environ. Res. Lett.* **17**, 054046. (doi:10.1088/1748-9326/ac68fa)
37. Chen G *et al.* 2020 Global projections of future urban land expansion under shared socioeconomic pathways. *Nat. Commun.* **11**, 537. (doi:10.1038/s41467-020-14386-x)
38. Tomasella J, Vieira RMSP, Barbosa AA, Rodriguez DA, de Oliveira Santana M, Sestini MF. 2018 Desertification trends in the Northeast of Brazil over the period 2000–2016. *Int. J. Appl. Earth Obs. Geoinf.* **73**, 197–206. (doi:10.1016/j.jag.2018.06.012)
39. Jamal S, Ahmad WS. 2020 Assessing land use land cover dynamics of wetland ecosystems using Landsat satellite data. *SN Appl. Sci.* **2**, 1891. (doi:10.1007/s42452-020-03685-z)
40. Dewitz J. 2021 National Land Cover Database (NLCD) 2019 Products (ver. 2.0): US Geological Survey data release. See https://doi.org/10.5066/P9KZCM54.
41. Stauffer D, Solomon S. 2007 Applications of physics and mathematics to social science. (http://arxiv.org/abs/0801.0121)
42. Koenig WD. 1999 Spatial autocorrelation of ecological phenomena. *Trends Ecol. Evol.* **14**, 22–26. (doi:10.1016/S0169-5347(98)01533-X)
43. Fajardo A, Velázquez E. 2021 Fine-scale spatial associations between functional traits and tree growth. *Oikos* **130**, 1988–2000. (doi:10.1111/oik.08376)
44. Gibbs JW. 1902 *Elementary principles in statistical mechanics: developed with especial reference to the rational foundations of thermodynamics*. New York, NY: Charles Scribner's Sons.
45. Jaynes ET. 1957 Information theory and statistical mechanics. *Phys. Rev.* **106**, 620–630. (doi:10.1103/PhysRev.106.620)
46. Metropolis N, Rosenbluth AW, Rosenbluth MN, Teller AH, Teller E. 1953 Equation of state calculations by fast computing machines. *J. Chem. Phys.* **21**, 1087–1092. (doi:10.1063/1.1699114)
47. Glauber RJ. 1963 Time-dependent statistics of the Ising model. *J. Math. Phys.* **4**, 294–307. (doi:10.1063/1.1703954)
48. D'Autilia R, Andrianaivo LN, Troiani A. 2021 Parallel simulation of two-dimensional Ising models using probabilistic cellular automata. *J. Stat. Phys.* **184**, 1–22. (doi:10.1007/s10955-021-02792-4)
49. Procacci A, Scoppola B, Scoppola E. 2016 Probabilistic cellular automata for low-temperature 2-d Ising model. *J. Stat. Phys.* **165**, 991–1005. (doi:10.1007/s10955-016-1661-2)
50. Kirkpatrick S, Gelatt Jr CD, Vecchi MP. 1983 Optimization by simulated annealing. *Science* **220**, 671–680. (doi:10.1126/science.220.4598.671)
51. Husmann K, Lange A, Spiegel E. 2017 The R package optimization: flexible global optimization with simulated-annealing.
52. Nowosad J. 2023 Spatialising: Ising model for spatial data. R package version 0.4.0. See https://github.com/Nowosad/spatialising.
53. Rosenfeld A, Pfaltz JL. 1966 Sequential operations in digital picture processing. *J. ACM* **13**, 471–494. (doi:10.1145/321356.321357)
54. Kumar V, Agrawal S. 2022 Urban modelling and forecasting of landuse using SLEUTH model. *Int. J. Environ. Sci. Technol.* **20**, 6499–6518. (doi:10.1007/s13762-022-04331-4)
55. Acheson J. 2008 Maine: on the cusp of the forest transition. *Human Organ.* **67**, 125–136. (doi:10.17730/humo.67.2.p84723j630q42620)
56. Lark TJ, Spawn SA, Bougie M, Gibbs HK. 2020 Cropland expansion in the United States produces marginal yields at high costs to wildlife. *Nat. Commun.* **11**, 4295. (doi:10.1038/s41467-020-18045-z)
57. Zhou L, Dang X, Sun Q, Wang S. 2020 Multi-scenario simulation of urban land change in Shanghai by random forest and CA-Markov model. *Sust. Cities Soc.* **55**, 102045. (doi:10.1016/j.scs.2020.102045)